OPTICS

Diffuse reflection and reciprocity-protected transmission via a random-flip metasurface

Hongchen Chu[1†], Xiang Xiong[1†], Ya-Jun Gao[1], Jie Luo[2], Hao Jing[1], Cheng-Yao Li[1], Ruwen Peng[1]*, Mu Wang[1,3]*, Yun Lai[1]*

Copyright © 2021 The Authors, some rights reserved; exclusive licensee American Association for the Advancement of Science. No claim to original U.S. Government Works. Distributed under a Creative Commons Attribution NonCommercial License 4.0 (CC BY-NC).

Rough surfaces lead to diffused light in both reflection and transmission, thereby blurring the reflected and transmitted images. Here, we merge the traditionally incompatible diffuse reflection and undistorted transmission by introducing the concept of random-flip metasurfaces made of randomly flipped components. These metasurfaces have a globally random phase in reflection that leads to diffuse reflection, while the local space inversion and reciprocity principle ensure distortion-free transmission. Notably, the metasurface reflects like a rough surface yet transmits like a smooth one in a broad spectrum. On the basis of complementary random arrays of gold nanorods, we verified this functionality by both optical spectroscopy and imaging experiments over a broad range of frequencies from the visible to the infrared regime. This feature, which originates from breaking the phase correlation between reflection and transmission by the metasurface, could enable a range of new optical materials and display technology.

INTRODUCTION

A rough surface causes diffuse reflection (*1*) and blurred transmission by destructing spatial phase coherence; in contrast, a flat surface allows specular reflection (*2*) and distortion-free transmission with uniform distribution of phase difference. Therefore, diffuse reflection and distortion-free transmission are usually incompatible. The consequences of this dilemma are the glare and reflective images that generally appear on the glass and the screens of the display devices, which often cover the transmitted images and even hurt the eyes. The antiglare coatings (*3*) using textured surfaces or suspended particles can reduce the glare but always at a substantial trade-off in the resolution and clarity of the transmitted scene. Here, we demonstrate a type of random-flip metasurfaces (RFMs) that may resolve this long-existing problem. These RFMs are composed of random distributions of two types of metasurface blocks related by the space inversion ("flip") operation. The reciprocity principle (*4*–*7*) and space inversion guarantee that these RFMs have distortion-free transmission despite the randomness. The random configurations only lead to the global random phase in reflection, which bestows diffuse reflection. Therefore, these RFMs can reflect light like rough optical surfaces yet transmit light like smooth surfaces in a broad bandwidth. By using an RFM made of complementary random arrays of gold nanorods, we have verified the coalescence of diffuse reflection and distort-free transmission through both optical spectroscopy and imaging experiments over a broad range of frequencies from the visible to the infrared regime. The specular reflection and reflective images are notably blurred, while the transmission remains almost intact, forming clear and sharp images. Our work reveals a unique mechanism to realize broadband unidirectional diffusion of light, which leaves the transmission "diffusion-immune." This breakthrough is a result of exploiting the space inversion and reciprocity principle in the metasurface design.

[1]National Laboratory of Solid State Microstructures, School of Physics, and Collaborative Innovation Center of Advanced Microstructures, Nanjing University, Nanjing 210093, China. [2]School of Physical Science and Technology, Soochow University, Suzhou 215006, China. [3]American Physical Society, 1 Research Road, Ridge, NY 11961, USA.
*Corresponding author. Email: laiyun@nju.edu.cn (Y.L.); rwpeng@nju.edu.cn (R.P.); muwang@nju.edu.cn (M.W.)
†These authors contributed equally to this work.

RESULTS

Theory and design of the RFM

In recent decades, metasurfaces have presented strong capabilities to manipulate light in unprecedented ways (*8*, *9*). On the basis of dedicated designing, the metasurfaces allow refraction and reflection beams to propagate toward any desired directions (*10*, *11*) and lead to many other intriguing functionalities (*12*–*18*). The application of fundamental physical principles in metasurfaces has generated many intriguing concepts such as the generalized laws of refraction and reflection (*10*, *11*), the Pancharatnam-Berry phase metasurface (*19*, *20*), Huygens' metasurface (*21*, *22*), etc. The reciprocity principle (*7*) is one of the most elegant principles in wave physics, which guarantees that the response of a reciprocal channel is symmetric when the source point and detection point are interchanged. On the other hand, the electromagnetic interactions are known to be invariant under the space inversion. In this work, we combine these two fundamental principles to design a new type of metasurfaces, i.e., RFMs, which can function as unprecedented optical surfaces that allow transmission of light like smooth surfaces and reflection of light like rough surfaces in a broad bandwidth. The concept is schematically shown in Fig. 1, where the reflection and transmission features of an ordinary flat glass (left), a frosted glass (middle), and an RFM (right) are illustrated, respectively. Intriguingly, the RFM functions like the frosted glass in reflection and like the flat glass in transmission. Therefore, the reflective imaging is prohibited, whereas the transmission images remain unblurred and distortion-free, forming the amazing phenomena illustrated in Fig. 1 (B and C).

To achieve the above phenomenon, randomness should be introduced to the reflection while leaving the transmission completely uninfluenced in a broad spectrum. This is a challenging task as the transmission and reflection are usually strongly coupled. To achieve this goal, we design the RFMs as composed of two types of metasurface blocks, hereby denoted as heads and tails, which are related to each other via the space inversion (flip) operation. Such two

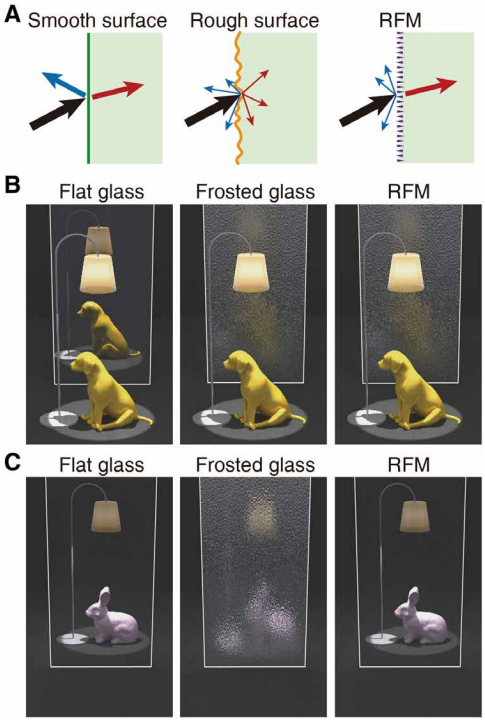

Fig. 1. The principle of RFMs and the visual effects in reflection and transmission. (**A**) shows that the RFM allows transmission like a smooth surface and reflection like a frosted surface. In (**B**) and (**C**) illustrations demonstrate the visual effects in reflection and transmission for a flat glass, a frosted glass, and an RFM, respectively. In (B), the illuminating lamp and the object are in front of the glass and metasurface, whereas in (C), they are behind the glass and metasurface.

elements may be schematically described as either "spin-up" or "spin-down," in analogy with the two spin states of electrons. We assume that the transmission and reflection coefficients of the head are described as t and r, respectively. The reciprocity principle asserts that when the incidence channel is switched with the transmission channel, as shown in Fig. 2A, the transmission coefficient will be exactly the same, i.e., $t' = t$. The reflection coefficient, however, will be largely different upon the switching, i.e., $r' \neq r$, when the head is asymmetric. In Fig. 2B, we demonstrate that by applying space inversion, the head structure is "flipped" into the tail structure. The transmission coefficient of the tail is exactly the same as that of the head, i.e., $t'' = t' = t$. This equivalence is strictly protected by the reciprocity principle and the space inversion, as long as the materials are reciprocal. It is inherently independent of the details of the head and tail structures, as well as the frequency and the incident angle. Contrarily, in reflection, we have $r'' = r' \neq r$, and generally, the phase difference between r' and r could be quite large over a broad spectrum. Last, to ensure that the incident and transmitted waves have the same polarization, the head and tail structures are designed to be symmetric in the plane of metasurface.

In the following, we demonstrate the transmission and reflection properties of three typical pairs of the heads and tails. The first example is a gold nanocone, as shown in Fig. 2C. The second example is composed of a gold nanoring and a gold nanorod, as shown in Fig. 2D. The third example is a gold nanorod shifted away from the center of the metasurface, as shown in Fig. 2E. These nanostructures are embedded inside a thin layer of silica substrate, and the geometry parameters are labeled in the figures. In the middle (right) of Fig. 2 (C to E), we demonstrate the transmittance (reflectance) and transmission (reflection) phase under normal incidence calculated by the finite-difference time-domain method. In all three cases, the transmission properties of the heads (I) and tails (II) are exactly the same in the broad visible and infrared spectrum, despite obvious frequency dispersions. Contrarily, the reflection properties of the heads and tails are distinctly different, because the spatial symmetry of the three examples is broken. These examples show the generality of this design strategy that combines the reciprocity principle and local space inversion (flip). Simulation proofs for other incident angles are shown in the Supplementary Materials. Because of the generality of the reciprocity principle and the transverse symmetry of the RFM structure, this effect also applies to both transverse-electric (TE) and transverse-magnetic (TM) polarizations (also shown in the Supplementary Materials).

When the heads and tails are ready, the next step is to arrange them randomly to form an RFM. In this work, we experimentally realize an optical RFM based on the design of the third example as shown in Fig. 2E. The final structure can be regarded as a double-layer metasurface constructed by overlapping two complementary random arrays of gold nanorods, as shown in Fig. 3A. The head (or tail) structure consists of 3 × 3 gold nanorods, as illustrated in Fig. 3B. Here, a 3 × 3 array of nanorods is adopted to preserve the reflection and transmission features of each nanorod obtained under the periodic conditions. The scale of the array is comparable to the wavelength. Thus, this design can avoid the homogenization of randomness in the deep subwavelength scale. In practice, the RFM is attached to a silica substrate; therefore, we reexamine the transmission and reflection with the substrate considered. As seen in Fig. 2C, the transmittance and transmission phase of the heads and tails are still almost identical in the wavelength regime from 400 to 1000 nm. The reflectances of the head and tail are also similar, while the reflection phase exhibits a notable difference, as shown in Fig. 3D. The efficiency of diffusion is maximized when the phase difference is $\Delta\phi \approx 180°$, which is achieved near 690 nm (denoted by a gray vertical line). In general, the phase difference is relatively large ($90° < \Delta\phi < 270°$) within a broad spectrum from 550 to 800 nm. Figure 3E shows the transmittance of the heads and tails as a function of the radius of the gold nanorods, R, at the condition of $\Delta\phi = 180°$. The transmittance through the RFM can be flexibly tuned by changing the radius R.

Here, we designate 1 and 0 to denote, respectively, the heads and tails illustrated in Fig. 3B. The random configuration of the RFM is characterized by a random binary map, as shown in the bottom left inset of Fig. 3A. For simplicity, the binary map follows the same random sequence in both x and y directions. Other random sequences can produce the similar effect of diffusion (Supplementary Materials). We note that the random distributions of different reflection phases have been applied to produce diffuse reflection for microwaves, optics, and acoustics previously (*23*–*26*). Here, the combined principle of the reciprocity principle and the space inversion inherently ensures that the transmission and reflection are, respectively, distortion-free and diffusive for optical waves of both polarizations in a broad bandwidth. Far-field radiation power patterns are obtained by full-wave simulations under the illumination of a TE Gaussian beam at various incident angles, as shown in Fig. 3F. In comparison, a pure-head metasurface (PHM) composed of only heads is also investigated. In the simulation, the RFM and PHM are both attached to a silica substrate, which is 1000 nm in thickness. A strong

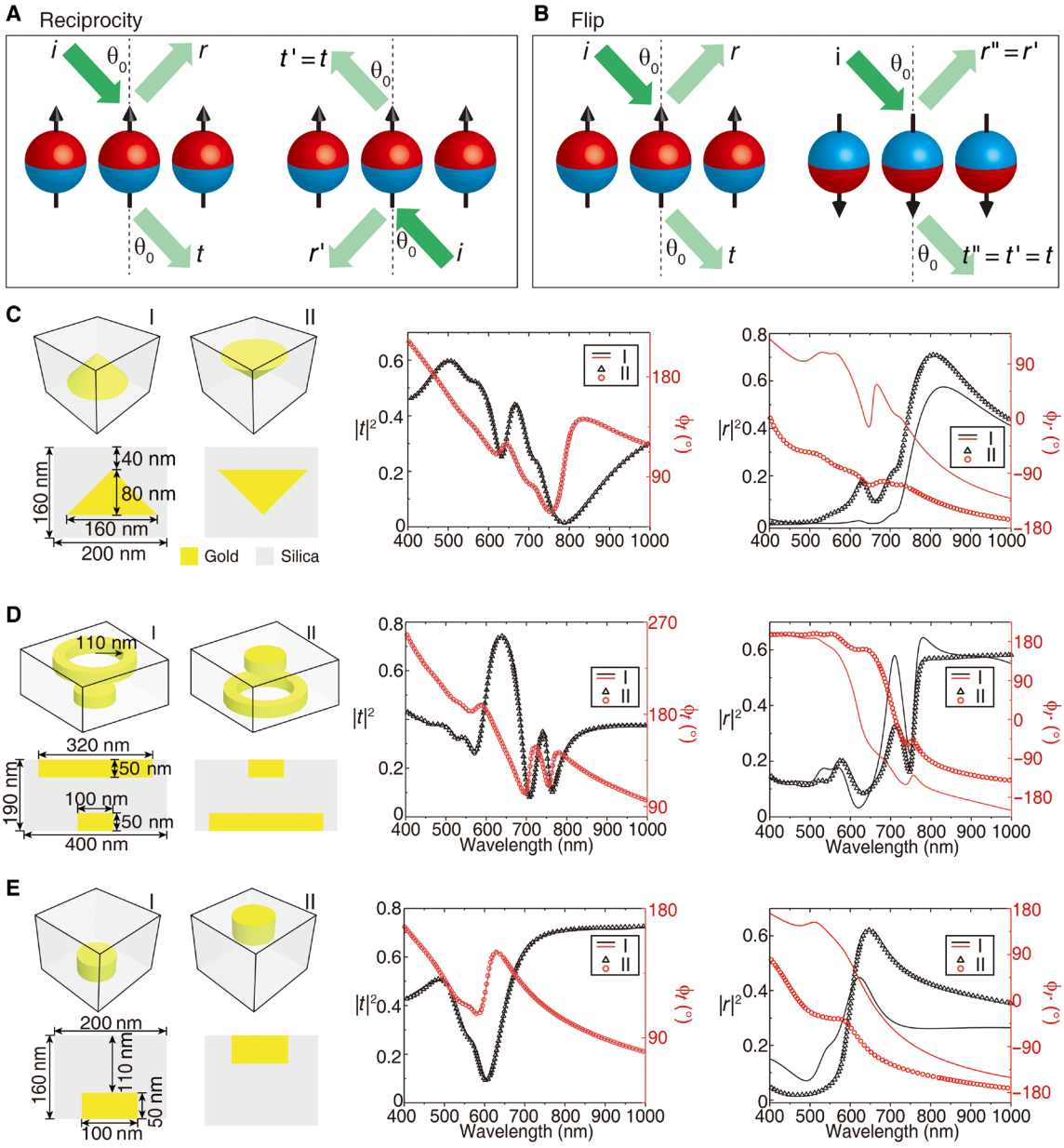

Fig. 2. The principle behind the metasurface component flip. Schematic diagrams of (**A**) the reciprocity principle and (**B**) transmission invariance under space inversion. Metasurface blocks composed of (**C**) an optical nanocone, (**D**) a pair of optical nanoring and nanorod, and (**E**) an optical nanorod with position shifted away from the center. Middle panels in (C) to (E) show the calculated transmittance and transmission phase, respectively, which prove the broadband identical transmission of the heads and tails protected by the reciprocity principle and space inversion. Right panels in (C) to (E) show the calculated reflectance and reflection phase, respectively, which show broadband large phase difference.

radiation lobe always appears in the direction of incidence, which corresponds to the transmission through the metasurface. It is nearly identical for the PHM and RFM, indicating that the random-flip configuration has almost no influence on transmission. Contrarily, on the reflection side, a large radiation lobe occurs for the PHM, which corresponds to the specular reflection. However, it is replaced by many small radiation lobes for the RFM. This proves that the reflection is distributed in various directions and much weaker than the specular reflection, which is the hallmark of diffuse reflection. The glare and reflective imaging on the RFM would be substantially reduced.

Fabrication and experimental demonstration

To verify the theoretical design, we fabricate the RFM by magnetron sputtering and electron beam lithography (EBL). The whole sample is around 340 μm by 340 μm in size, consisting of 70 × 70 repetitions of the structure shown in Fig. 3A. Figure 4A shows the scanning electron micrographs (SEMs) of the sample. For comparison, a PHM sample of the same size is also fabricated. We first measure the transmission and reflection intensity images of the samples under the illumination of a 695-nm laser beam by using a charge-coupled device (CCD) camera mounted on a microscope. Figure 4B shows the intensity profiles of the beams corresponding to the transmission

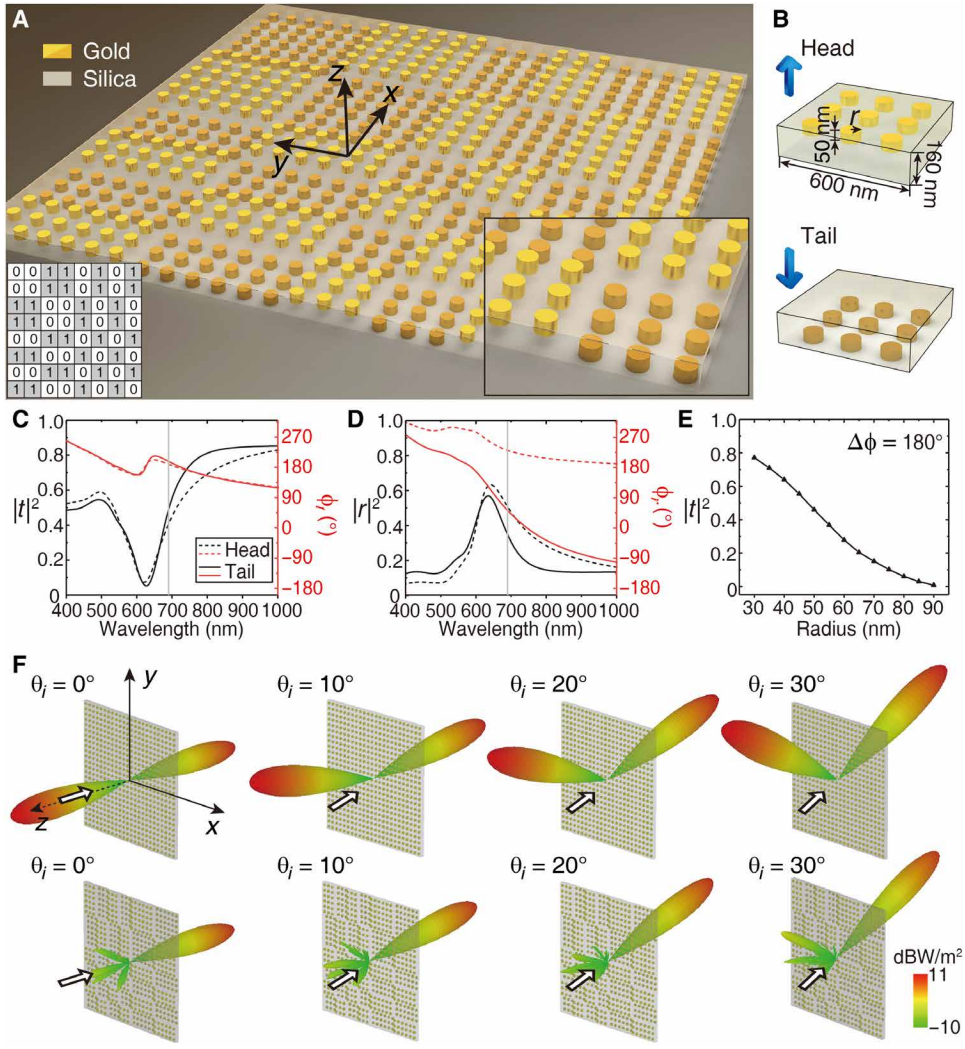

Fig. 3. The design of an RFM and the numerical verifications. (**A**) Three-dimensional illustration of a double-layer RFM based on two complementary arrays of gold nanorods, which can be regarded as a random binary map (the bottom left inset) of the heads and tails. The bottom right inset shows a zoom-in view of the corner of the RFM. (**B**) The detailed structures of the heads and tails. (**C**) Transmittance and transmission phase of the heads and tails. (**D**) Reflectance and reflection phase of the heads and tails. (**E**) Transmittance at the condition of $\Delta\phi = 180°$ as a function of the radius of the gold nanorods. (**F**) Far-field radiation power patterns for a PHM (top) and an RFM (bottom) under the illumination of a TE-polarized Gaussian beam at the incident angle (marked by white arrow) of $\theta_i = 0°$, 10°, 20°, and 30°, respectively.

and specular reflection. The transmission images through the RFM and PHM are almost identical. Contrarily, the specular reflection image from the RFM is substantially weaker than that from the PHM. Quantitative measurement of the light power indicates that the difference is over one order of magnitude (1.0 μW versus 14.2 μW). This proves that the optical energy of specular reflection is largely reduced due to the redistribution of power to other directions by the RFM. We then measure the far-field intensity profiles of the RFM and PHM samples using the setup shown in Fig. 4C. A 695-nm laser beam is incident on the sample at the angle θ_i, and the scattered light at the angle θ is detected by a spectrometer, which is mounted on a rotation stage in the plane of incidence. Figure 4D shows the measured far-field intensity profiles for $\theta_i = 10°$, 20°, and 30° by a spectrometer, respectively. High transmittance is always observed for both RFMs and PHMs. The specular reflection from the RFM is substantially reduced by 92.6, 92.7, and 80.1% in comparison with that from the PHM, for $\theta_i = 10°$, 20°, and 30°, respectively. Through increasing the size of the RFM, the optical diffuse reflection in principle could be further optimized and work for even larger incident angles.

The formation of images in transmission and reflection is investigated by the setups shown in Fig. 5A. The wavelength of the illuminating light is chosen by bandpass filters with different central wavelengths. A rabbit cartoon and a dog cartoon with the typical linewidths of 4 μm (Fig. 5B) are created by EBL and used as the objects for transmission and reflection, respectively. The cartoons are placed either 0.7 mm below (transmission setup) or 1.4 mm above (reflection setup) the metasurfaces. For each wavelength, the photo images of the cartoons are taken with the same camera parameters under the same illuminating light for the RFM and PHM samples. In Fig. 5C, the images of the rabbit taken in the transmission setup are demonstrated for different wavelengths ranging from 520 to 850 nm. They are all clear and sharp for both the RFM and PHM. This indicates that the transmission is distortion-free and

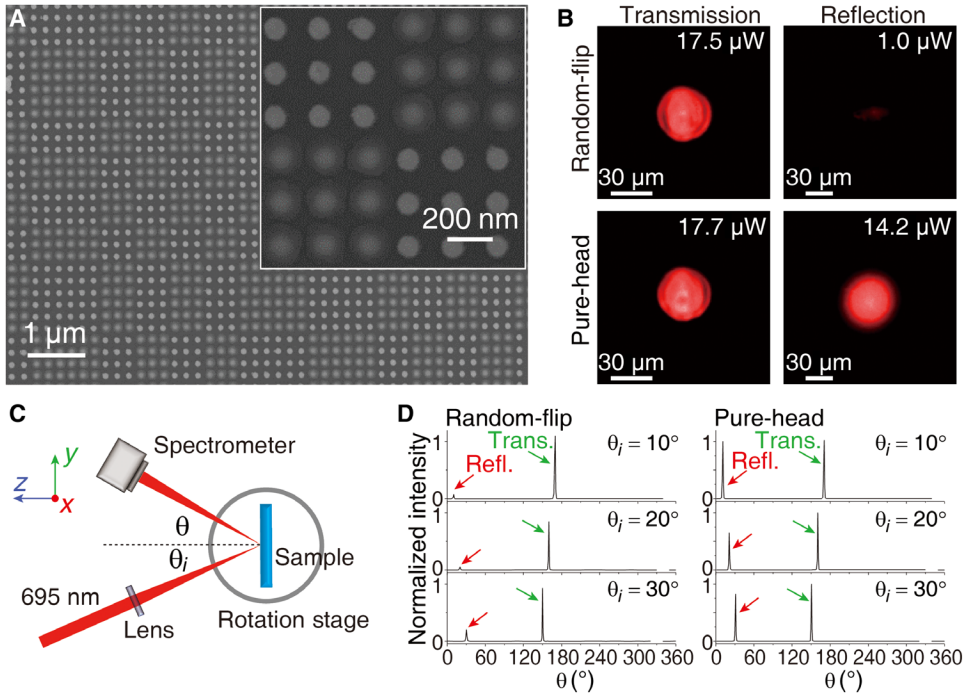

Fig. 4. Transmission and reflection experiments for the RFM and PHM. (**A**) SEM images of a part of the fabricated RFM. The inset graph shows the zoom-in view of the RFM. (**B**) The intensity profiles of the transmitted (left column) and reflected beams (right column) for the RFM (top) and PHM (bottom). The incident laser beam is controlled by an aperture diaphragm. The measured optical power is depicted in the corresponding panels. (**C**) Schematic graph of the angular distribution measurement setup. (**D**) The measured angular distributions of the light intensity for the RFM and PHM under the incident angles of 10°, 20°, and 30°, respectively.

unaffected by the randomness over a broad visible and infrared spectrum. Figure 5D demonstrates the images of the dog that were taken in the reflection setup. The dog pattern is difficult to recognize in the images taken for the RFM at the same wavelengths from 520 to 850 nm due to the diffused reflection. In contrast, it remains clear and sharp in the images taken for the PHM, as a consequence of the mirror reflection. The working bandwidth extends from the visible spectrum into the infrared regime. In Fig. 5E, we further demonstrate the transmitted images of the USAF 1951 resolution test chart through the RFM, where the ability to resolve the element 6 of group 7 is observed at all frequencies. The clear images in transmission and disappearing images in reflection confirm that the RFM bestows the amazing phenomenon of coexisting diffuse reflection and distortion-free transmission.

DISCUSSION

We should emphasize that the design strategy demonstrated here is universal. As discussed in Fig. 2, the diffuse reflection and distortion-free transmission of the RFM do not depend on either the specific shape or the material components of the heads and tails in the RFM. Any reciprocal structures that are distinguishable under the flip operation can be applied to construct the RFM. Since the loss cannot break reciprocity, this principle inherently applies to absorptive structures like metals. Moreover, the RFM structure can be further optimized or simplified to match with the industry-level optical lithography, such that mass production of RFMs is potentially feasible. It is worth noting that besides the effect of diffuse reflection, other functions of binary-phase optical elements, such as binary phase zone plates and phase gratings, can also be integrated into the flip-type metasurfaces.

As we have shown in Fig. 3E, the transmittance of the RFM is flexibly tunable from over 90% to near zero. The absorption of the RFM is also configurable in the design. Therefore, the transmission, reflection, and absorption of the RFMs can all be customized as needed, without affecting the core functionality of diffuse reflection and distortion-free transmission. Comparing with Huygens' metasurfaces (*21*, *22*) and antireflection coatings (*27*–*30*) that eliminate the reflection based on transmission or absorption enhancement, the tunable transmission of RFMs offers greater flexibility in many scenarios where low transmittance is more favorable than the high one, such as the glass curtain walls.

From the aspect of diffusion theory, the RFM introduces the phenomenon of unidirectional diffusion. The optical diffuse scattering is confined in the reflection channel only. In the transmission channel, the light is unaffected by the random configuration, and therefore, all the carried information is completely preserved. This is in sharp contrast with current antiglare structures such as rough matt surfaces, in which the transmitted images are always blurred to a certain extent due to the inevitable diffusion of transmitted light. In principle, RFMs may provide an antiglare solution for future high-definition displays, vehicle glasses, etc.

We note that the diffusing of light does not necessarily require a $\Delta\phi \approx 180°$ phase difference in the reflection from the head and tail structures (as also discussed in the Supplementary Materials), which renders the broadband diffusion behavior despite the resonant nature of the RFM. The diffusion efficiency can be further improved by extending the bandwidth of maximized phase difference in reflection. On the other hand, the protection of transmission by the reciprocity principle and space inversion is almost frequency independent. These broadband characteristics together lead to the

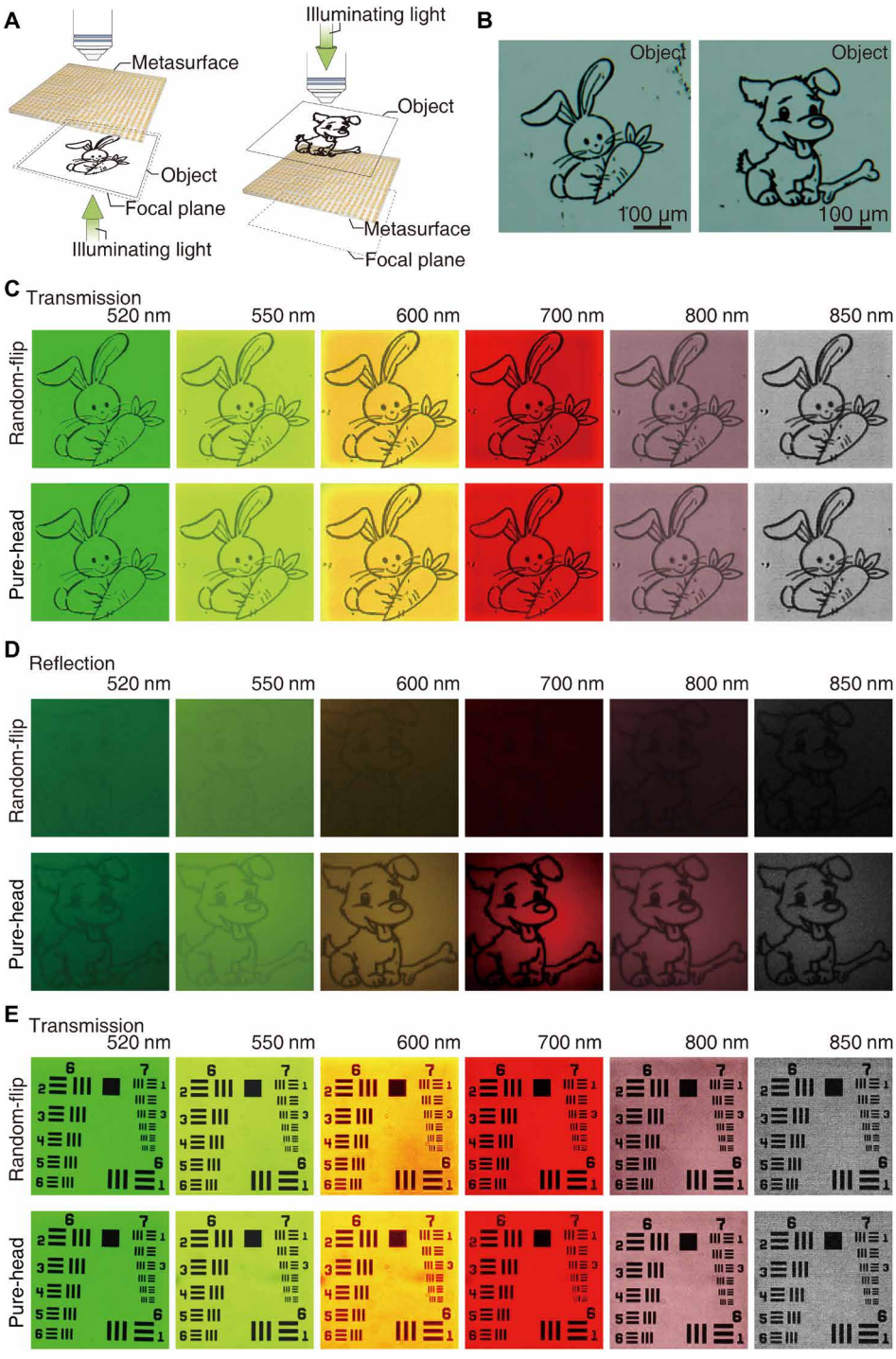

Fig. 5. Imaging experiments for the RFM and PHM. (**A**) The schematic graphs of the measurement setups in transmission (left) and reflection (right), respectively. (**B**) The optical photographs of the rabbit and dog patterns, which are used as the objects in transmission and reflection, respectively. (**C** and **D**) The photo images captured with a microscope from the RFM (top) and PHM (bottom) in the transmission (C) and reflection (D) setups, respectively. (**E**) The photo image of a USAF 1951 resolution test chart captured from the RFM in the transmission setup. The central wavelengths of the illuminating light are 520 nm, 550 nm, 600 nm, 700 nm, 800 nm (false color), and 850 nm (false color), respectively.

broadband coalescence of diffuse reflection and distortion-free transmission. With the unique ability of reflecting like rough surfaces and transmitting like smooth surfaces, the RFMs represent an unprecedented type of optical surfaces that guarantee perfectly clean optical display and simultaneous elimination of the specular reflection via optical diffusion. Hence, the demonstrated RFMs may find broad applications in many practical scenarios, such as display screens, glass curtain walls of buildings, and vehicle glass, where the

clear vision is desired while the disturbing glare stemming from specular reflection prefers to be eliminated.

MATERIALS AND METHODS

Fabrication of the RFMs

First, gold rods in tail blocks of RFM are fabricated on a fused silica substrate with a thickness of 0.7 mm by EBL. Then, a 160-nm-thick fused silica layer deposits on the gold rods and substrate by magnetron sputtering. Afterward, again, EBL is adopted to fabricate gold rods of head blocks on the deposited fused silica layer. Last, a 50-nm-thick fused silica layer deposits on the top to cover the exposed gold rods. Fused silica bumps on gold rods stemming from the deposition progress are not shown in Fig. 3 but are taken into consideration in all numerical simulations. PHM is fabricated in a similar way, except that all gold rods are fabricated at once in one layer.

SUPPLEMENTARY MATERIALS

Supplementary material for this article is available at https://science.org/doi/10.1126/sciadv.abj0935

REFERENCES AND NOTES

1. E. Hecht, *Optics* (Pearson, ed. 5, 2017), pp. 105–108.
2. J. M. Enoch, History of mirrors dating back 8000 years. *Optom. Vis. Sci.* **83**, 775–781 (2006).
3. A. M. Nuijs, J. J. Horikx, Diffraction and scattering at antiglare structures for display devices. *Appl. Optics* **33**, 4058–4068 (1994).
4. A. T. de Hoop, Reciprocity of the electromagnetic field. *Appl. Sci. Res. B* **8**, 135–140 (1959).
5. R. J. Potton, Reciprocity in optics. *Rep. Prog. Phys.* **67**, 717–754 (2004).
6. Y. Shi, Z. Yu, S. Fan, Limitations of nonlinear optical isolators due to dynamic reciprocity. *Nat. Photonics* **9**, 388–392 (2015).
7. D. L. Sounas, A. Alù, Non-reciprocal photonics based on time modulation. *Nat. Photonics* **11**, 774–783 (2017).
8. N. Yu, F. Capasso, Flat optics with designer metasurfaces. *Nat. Mater.* **13**, 139–150 (2014).
9. A. V. Kildishev, A. B. Oltasseva, V. M. Shalaev, Planar photonics with metasurfaces. *Science* **339**, 1232009 (2013).
10. N. Yu, P. Genevet, M. A. Kats, F. Aieta, J. P. Tetienne, F. Capasso, Z. Gaburro, Light propagation with phase discontinuities: Generalized laws of reflection and refraction. *Science* **334**, 333–337 (2011).
11. X. Ni, N. K. Emani, A. V. Kildishev, A. Boltasseva, V. M. Shalaev, Broadband light bending with plasmonic nanoantennas. *Science* **335**, 427 (2012).
12. M. Khorasaninejad, F. Capasso, Metalenses: Versatile multifunctional photonic components. *Science* **358**, eaam8100 (2017).
13. S. Sun, Q. He, S. Xiao, Q. Xu, X. Li, L. Zhou, Gradient-index meta-surfaces as a bridge linking propagating waves and surface waves. *Nat. Mater.* **11**, 426–431 (2012).
14. G. Zheng, H. Mühlenbernd, M. Kenney, G. Li, T. Zentgraf, S. Zhang, Metasurface holograms reaching 80% efficiency. *Nat. Nanotechnol.* **10**, 308–312 (2015).
15. N. K. Grady, J. E. Heyes, D. R. Chowdhury, Y. Zeng, M. T. Reiten, A. K. Azad, A. J. Taylor, D. A. R. Dalvit, H. T. Chen, Terahertz metamaterials for linear polarization conversion and anomalous refraction. *Science* **340**, 1304–1307 (2013).
16. X. Yin, Z. Ye, J. Rho, Y. Wang, X. Zhang, Photonic spin hall effect at metasurfaces. *Science* **339**, 1405–1407 (2013).
17. N. Shitrit, I. Yulevich, E. Maguid, D. Ozeri, D. Veksler, V. Kleiner, E. Hasman, Spin-optical metamaterial route to spin-controlled photonics. *Science* **340**, 724–726 (2013).
18. X. Ni, Z. J. Wong, M. Mrejen, Y. Wang, X. Zhang, An ultrathin invisibility skin cloak for visible light. *Science* **349**, 1310–1314 (2015).
19. D. Lin, P. Fan, E. Hasman, M. L. Brongersma, Dielectric gradient metasurface optical elements. *Science* **345**, 298–302 (2014).
20. F. Cardano, L. Marrucci, Spin-orbit photonics. *Nat. Photonics* **9**, 776–778 (2015).
21. C. Pfeiffer, A. Grbic, Metamaterial Huygens' surfaces: Tailoring wave fronts with reflectionless sheets. *Phys. Rev. Lett.* **110**, 197401 (2013).
22. I. Staude, A. E. Miroshnichenko, M. Decker, N. T. Fofang, S. Liu, E. Gonzales, J. Dominguez, T. S. Luk, D. N. Neshev, I. Brener, Y. Kivshar, Tailoring directional scattering through magnetic and electric resonances in subwavelength silicon nanodisks. *ACS Nano* **7**, 7824–7832 (2013).
23. T. J. Cui, M. Q. Qi, X. Wan, J. Zhao, Q. Cheng, Coding metamaterials, digital metamaterials and programmable metamaterials. *Light Sci. Appl.* **3**, e218 (2014).
24. L. Gao, Q. Cheng, J. Yang, S. Ma, J. Zhao, S. Liu, H. Chen, Q. He, W. Jiang, H. Ma, Q. Wen, L. Liang, B. Jin, W. Liu, L. Zhou, J. Yao, P. Wu, T. Cui, Broadband diffusion of terahertz waves by multi-bit coding metasurfaces. *Light Sci. Appl.* **4**, e324 (2015).
25. Y. Zhu, X. Fan, B. Liang, J. Cheng, Y. Jing, Ultrathin acoustic metasurface-based schroeder diffuser. *Phys. Rev. X* **7**, 021034 (2017).
26. Z. Li, Q. Dai, M. Q. Mehmood, G. Hu, B. L. Yanchuk, J. Tao, C. Hao, I. Kim, H. Jeong, G. Zheng, S. Yu, A. Alù, J. Rho, C. Qiu, Full-space cloud of random points with a scrambling metasurface. *Light-Sci. Appl.* **7**, 63 (2018).
27. M. Born, E. Wolf, *Principles of Optics* (Cambridge Univ. Press, 2003).
28. S. Walheim, E. Schaffer, J. Mlynek, U. Steiner, Nanophase-separated polymer films as high-performance antireflection coatings. *Science* **283**, 520–522 (1999).
29. H. T. Chen, J. Zhou, J. F. O'Hara, F. Chen, A. K. Azad, A. J. Taylor, Antireflection coating using metamaterials and identification of its mechanism. *Phys. Rev. Lett.* **105**, 073901 (2010).
30. K. Im, J. Kang, Q. Park, Universal impedance matching and the perfect transmission of white light. *Nat. Photonics* **12**, 143–149 (2018).
31. J. M. Vigoureux, R. Giust, Explicit Stokes reciprocity relations for plane stratified media. *Opt. Commun.* **176**, 1–8 (2000).
32. P. B. Johnson, R. W. Christy, Optical constants of the noble metals. *Phys. Rev. B* **6**, 4370–4379 (1972).

Acknowledgments

Funding: This work was supported by the National Key R&D Program of China grant 2020YFA0211300 (to M.W., R.P., X.X., and Y.L.), National Key R&D Program of China grant 2017YFA0303702 (to M.W., R.P., and X.X.), National Natural Science Foundation of China grant 12174188 (to Y.L.), National Natural Science Foundation of China grant 11974176 (to Y.L.), National Natural Science Foundation of China grant 11634005 (to R.P.), National Natural Science Foundation of China grant 11974177 (to M.W.), National Natural Science Foundation of China grant 61975078 (to R.P.), and National Natural Science Foundation of China grant 11704271 (to J.L.). **Author contributions:** H.C. and X.X. contributed equally to this work. Y.L., R.P., and M.W. organized and led the project. H.C. designed the metasurface and performed the theoretical analysis. X.X. fabricated the metasurface samples and performed the optical measurement. Y.-J.G., H.J., and C.-Y.L. helped in the experiments. J.L. helped in the analysis. H.C., Y.L., M.W., R.P., and X.X. prepared the manuscripts. **Competing interests:** The authors declare that they have no competing interests. **Data and materials availability:** All data needed to evaluate the conclusions in the paper are present in the paper and/or the Supplementary Materials.

Submitted 20 April 2021
Accepted 16 July 2021
Published 8 September 2021
10.1126/sciadv.abj0935

Citation: H. Chu, X. Xiong, Y.-J. Gao, J. Luo, H. Jing, C.-Y. Li, R. Peng, M. Wang, Y. Lai, Diffuse reflection and reciprocity-protected transmission via a random-flip metasurface. *Sci. Adv.* **7**, eabj0935 (2021).